

Microscopic Models of Heavy Ion Interactions

A. Capella

*Laboratoire de Physique Théorique (UMR CNRS N° 8627),
Université Paris XI, Bâtiment 210, 91405 Orsay Cedex, France,
E-mail : alphonse.capella@th.u-psud.fr*

Abstract

An introduction to dynamical microscopic models of hadronic and nuclear interactions is presented. Special emphasis is put in the relation between multiparticle production and total cross-section contributions. In heavy ion collisions, some observables, considered as signals of the production of a Quark Gluon Plasma (QGP), are studied. It is shown that they can only be described if final state interactions are introduced. It is argued that the cross-sections required are too small to drive the system to thermal equilibrium within the duration time of the final state interaction.

LPT Orsay 03-36
May 2003

*Lectures at VIII Hispalensis International Summer School, Séville (Spain),
to be published by Springer Verlag*

1 Introduction

Statistical QCD predicts the existence of new states of matter at high temperature T and high baryon number densities μ (baryochemical potential). The phase diagram is schematically represented in Fig. 1. Let us discuss first the phase transition at high T and small μ (i.e. when baryon and antibaryon densities are approximately equal). At $\mu = 0$, lattice calculations [1] show a phase transition to a deconfined plasma of quarks and gluons (QGP) at a critical temperature $T_c \sim 150 \div 200$ MeV, corresponding to an energy density ε – an order of magnitude higher than that of ordinary nuclear matter ($\varepsilon_0 = 170$ MeV/fm³). The results are shown in Fig. 2. Below the critical temperature T_c , we heat the system and the temperature increases towards T_c . At $T \sim T_c$, the temperature remains constant (the energy given to the system is used to increase its latent heat) and the energy density ε increases sharply. For $T > T_c$ the temperature increases again with ε/T^4 approximately constant, as it should be for an ideal gas (Stefan-Boltzmann limit). The sharp increase of ε/T^4 near T_c is due to the increase in the number of degrees of freedom of the system from a hadronic phase ($T < T_c$) to a plasma of quarks and gluons ($T > T_c$).

In the ideal case of pure gauge QCD (the so-called “quenched” approximation in which dynamical quarks are absent) the phase transition is first order. In the presence of dynamical quarks the situation is more complicated and the order of the phase transition depends on the number of flavors. A restoration of chiral symmetry also takes place at the same T_c .

The region $\mu \sim 0$ studied in lattice QCD corresponds to the conditions in high-energy heavy ion collisions at mid-rapidities. It also corresponds to the conditions in the primordial universe. In the opposite conditions, i.e. low temperature and high baryon densities (i.e. the conditions at the center of neutron stars) a new phase (or phases) is expected [2] producing a color superconductor in which pairs of quarks condensate – in a way similar to electron (Cooper) pairs in QED.

A possibility to create in the laboratory the high energy densities and temperatures required for the production of QGP is via head-on heavy ion collisions at high energy. In AA collisions, the energy density can be evaluated using the Bjorken formula

$$\varepsilon \sim \left(\frac{dN}{dy} \right)_{y^* \sim 0}^{hadrons} \frac{\langle m_T \rangle}{\tau_0 \pi R_A^2} .$$

Here dN/dy is the number of produced hadrons per unit rapidity and $\langle m_T \rangle$ is their average energy. R_A is the nuclear radius and τ_0 an average formation time. Taking the customary value $\tau_0 \sim 1$ fm, we obtain for central $Au Au$ collisions at RHIC an energy density $\varepsilon \sim 4$ GeV/fm³, which appears to be high enough for QGP production.

Does it mean that QGP production in high-energy heavy ion collisions follows from QCD ? The answer is negative. Indeed, QGP formation is predicted by statistical QCD, i.e. QCD applied to a system in thermal equilibrium. Therefore, one of the main issues in heavy ion physics is to determine whether the produced final state reaches thermal equilibrium. This depends, of course, on the strength and time duration of the final state interaction and can only be decided with the help of experiment. The observables which provide the most reliable information are the so-called signals of QGP. In this lecture I will discuss two of the most important signals : the particle abundance (in particular, hyperon and antihyperon production) and the J/ψ suppression. The latter could be due to the deconfinement or “melting” of the $c\bar{c}$ bound state in the plasma [3]. However, a similar phenomenon is observed in pA collisions, where the produced densities are too small for QGP formation. As for the former, an argument in favor of equilibrium is the fact that particle abundances are well described using statistical models [4]. Moreover, these models provide a natural explanation [5] of the increase of the relative yields of strange particles in central nucleus-nucleus as compared to pp collisions (strangeness enhancement). However, one should take into account that these models are also very successful [6] in pp and even in e^+e^- interactions, where QGP is not produced.

Therefore, it is important to study these observables in the framework of microscopic models which are successful in describing pp and pA interactions and can be generalized to heavy ion collisions. Models of this type [7-10] are called string models, in which particle production takes place in the form of strings (chromo-electric flux tubes) stretched between constituents of complementary color charge. In QCD, the force between complementary color charges (such as a quark and an antiquark of same color), are small at distances smaller than the hadron radius. However, at larger distances, the potential of the chromo-electric field increases linearly with the distance (confinement). Due to the strong force generated by this potential it is not possible to isolate the two color charges. Indeed, in the attempt to separate them, the potential energy of the system increases very rapidly and is converted into mass via the creation of quark-antiquark pairs. This results in the production of hadrons (mostly mesons), formed by recombination of a quark and an antiquark of adjacent pairs. The lines of force of the chromo-electric field are strongly colimated along the axis determined by the two color charges. Hence the string-like or jet-like shape of the set of produced hadrons.

As a starting point, one usually assumes in these models that particles produced in different strings are independent. In this case thermal equilibrium cannot be reached, no matter how large the energy density is. Indeed, in this case a large energy-density is the result of piling up a large number of independent strings. In other words, some “cross-talk” between different strings is needed in order to thermalize the system.

The assumption of independence of strings works remarkably well in hh and

hA interactions [7-10] – even in the case of event samples with 5 or 6 times the average multiplicity – indicating that no sizable final state interaction is present in these reactions. However, it is clear that in heavy ion collisions, where several strings occupy a transverse area of 1 fm^2 , the assumption of string independence has to break down. This is indeed the case. As we shall see, some data cannot be described without final state interaction. It could have happened that this final state interaction is so strong that the string picture breaks down and becomes totally useless. This does not seem to be the case. On the contrary, present data can be described using the particle densities computed in the model as initial conditions in the gain and loss (transport) equations governing the final state interaction. The interaction cross-section turns out to be small (a few tenths of a mb). Due to this smallness and to the limited interaction time available, final state interaction has an important effect only on rare processes, in particular Ξ , Ω and J/ψ production, or particle yields at large p_T . The bulk of the final state is not affected.

The plan of these lectures is as follows : in Section 2, I introduce the general framework of high-energy scattering in a hadronic language with special emphasis on the unitarity condition and its implementation in eikonal and Glauber Models. This section contains also some rudiments of Regge poles and the concept of Pomeron. In Section 3, I introduce a microscopic model : the Dual Parton Model (DPM) and compute the charged particle multiplicities as a function of energy and centrality (the latter characterizes the impact parameter of the collision in a way which is experimentally measurable). In Section 4, I study the so-called stopping power, i.e. the fate of the nucleons of the colliding nuclei. Particle abundances are studied in Section 5 and J/ψ suppression in Section 6. Section 7 contains the conclusions.

2 High-Energy Scattering : Hadronic Picture

2.1 General Framework

An important property of strong interactions is the unitarity of the S matrix operator

$$SS^+ = S^+S = 1 . \tag{1}$$

The S matrix is the operator that transforms free states at time $t = -\infty$ into free states at times $t = +\infty$. If we write

$$S = 1 + iT , \tag{2}$$

where $\langle a|T|b \rangle$ is the transition amplitude between free states a and b , the unitarity condition (1) reads

$$2 \operatorname{Im} \langle a|T|b \rangle = \sum_{\text{all } n} \langle a|T|n \rangle \langle n|T|b \rangle^* . \quad (3)$$

Here n denotes any state that can be reached from both a and b . For a identical to b , eq. (3) reduces to

$$2 \operatorname{Im} \langle a|T|a \rangle = \sum_{\text{all } n} (\langle a|T|n \rangle)^2 . \quad (4)$$

A two body amplitude $1 + 2 \rightarrow 3 + 4$ depends on two independent variables :

$$s = (p_1 + p_2)^2 , \quad t = (p_1 - p_3)^2 , \quad u = (p_1 - p_4)^2 , \quad (5)$$

with $s + t + u = m_1^2 + m_2^2 + m_3^2 + m_4^2$. When a and b are identical, $t = 0$. Since the sum in the r.h.s. of (4) builds up the total $1 + 2$ cross-sections, we obtain from (4) the optical theorem, which relates the total cross-section to the forward ($t = 0$) imaginary part of the elastic amplitude $T_{el}(s, t)$

$$\sigma_{tot}(s) = \frac{4\pi}{s} \operatorname{Im} T_{el}(s, t = 0) . \quad (6)$$

Let us now examine some of the implications of the unitarity condition (4). It is convenient to separate the states n into two classes. The first class consists of all inelastic states containing no large rapidity gap between the produced particles. The second class consists of those events with at least one large rapidity gap. Obviously, elastic scattering produces a state of the second class. We know experimentally that the first class of events gives the most important contribution to the total cross-section. It is convenient to depict such a contribution in the form of a diagram as shown in Fig. 3a. (Its interpretation will be discussed below). The important point is that the final state in Fig. 3a has also to be included as intermediate state in 4. This is precisely the contribution of the elastic state which, as discussed above, belongs to the second class of intermediate states. One obtains in this way the diagram shown in Fig. 3b. Here the lines with a cross denote the contribution of the on-shell initial state to the elastic amplitude. Repeating such an iteration, one is led to the multiple scattering diagram depicted in Fig. 3c. One has to add up all the diagrams in Figs. 3. In fact, inelastic states (for instance pN^* and N^*N^* in the case of pp scattering) also contribute as intermediate states, so that the vertex function (blob) of the diagrams in Fig. 3b and 3c can be quite complicated. There are also contributions due to intermediate states n containing more than one rapidity gap. However, their contributions are small at present energies and will not be considered here.

The interpretation of the diagram in Fig. 3a originates from the claim that the inelastic intermediate states (without rapidity gap) generate a Regge pole called the

Pomeron (see Section 2.5). All diagrams can be treated as Feynman diagrams in a field theory called Reggeon Field Theory or Gribov's Reggeon Calculus [11]. When only the diagrams in Figs. 3 are kept, one obtains, as a particular case, the so-called eikonal model for hadron-hadron scattering or the Glauber model in interactions involving nuclei.

2.2 The Eikonal and Glauber Models

In the case of hadron-hadron interactions the diagram in Fig. 3a (Pomeron) is also called the Born term. Its contribution to the total cross-section is parametrized in the form $g_{13}(t)g_{24}(t)s^\Delta$ where g are coupling constants and Δ a parameter (see Section 2.5). Let us consider the case of pp scattering and let us assume for simplicity an exponential dependence, in t , i.e.

$$g_{13}(t) = g_{24}(t) = A \exp(Bt) . \quad (7)$$

In this case, all loop integrals in Figs. 3b and 3c can be performed analytically. At a given s there are only two free parameters A^2s^Δ and B , which can be determined from the experimental values of σ_{tot} and σ_{el} (or from σ_{tot} and the slope of the elastic amplitude). For s variable there is a third parameter Δ , and the values of σ_{tot} and σ_{el} at several energies can be described in this way.

A contribution to the total cross-section in s^Δ with $\Delta > 0$ violates the Froissard bound [12] (consequence of unitarity). Note that $\Delta > 0$ is needed in order to describe the rise with energy of σ_{tot} . However, when all multiple scattering terms are added, one obtains, at high energy, $\sigma_{tot} \propto \ell n^2 s$, i.e. the maximal increase with s allowed by the Froissard bound.

It is convenient to work in the impact parameter (b) representation. The scattering amplitude in b -space is defined as $T(s, b) = (1/2\pi) \int d^2q_T \exp(-i\vec{q}_T \cdot \vec{b})T(s, t)$ where $t = -q_T^2$. Using this transformation it is easy to see that at fixed b the contribution of a diagram involving n exchanges (Fig. 3c) is just the n -th power of the Born term (Fig. 3a) times some trivial combinatorial factors. Furthermore the sum over n has a simple expression (see below, footnote 1). All these features will now be described in detail in the case of the Glauber model.

Let us consider, for definiteness, a proton-nucleus (pA) scattering. In this case there are no free parameters involved. Indeed, the t -dependence (or b -dependence) of the proton vertex function can be neglected in comparison with the fast variation of the nuclear one. The latter is known from the nuclear density. Moreover, in this case the Born term at $t = 0$ is just the inelastic proton-nucleon cross-section, which is known experimentally. The main formula of the probabilistic Glauber model is the one that gives the cross-section σ_n for n inelastic collisions of the projectile with n nucleons of the target nucleus (the remaining $A - n$ nucleon which do not participate in the interaction are called spectators), at fixed impact parameter b :

$$\sigma_n(b) = \binom{A}{n} (\sigma_{inel} T_A(b))^n (1 - \sigma_{inel} T_A(b))^{A-n} . \quad (8)$$

Here σ_{inel} is the proton-nucleon inelastic cross-section and $T_A(b)$ is the nuclear profile function (obtained by integrating the nuclear density : $T_A(b) = \int_{-\infty}^{+\infty} dZ \rho_A(Z, b)$; $\int d^2b T_A(b) = 1$). Equation (8) is just the Bernoulli's formula for composite probabilities. The first factor is a trivial combinatorial factor corresponding to the different ways of choosing n nucleons out of A . The second one gives the probability of having n inelastic pN collisions at given b . The third one is the probability that the remaining $A - n$ nucleons do not interact inelastically. Let us consider first a term with two collisions both of which are inelastic. The corresponding cross-section is $\sigma_2^2(b) = \binom{A}{2} (\sigma_{inel} T_A(b))^2$ i.e. a positive term. Let us now consider the case of two collisions only one of which is inelastic. The corresponding (interference) term is $\sigma_2^1(b)$ obtained from Eq. (8) by putting $n = 1$ and taking the second term in the expansion of the last factor. We get $\sigma_2^1(b) = -A(A - 1)(\sigma_{inel} T_A(b))^2$. We see that $\sigma_2^1(b) = -2\sigma_2^2(b)$. Thus, a rescattering term containing two collisions gives a negative contribution to the total pA cross-section.

Let us now consider their contributions to $d\sigma/dy$. They are given by $\sigma_2^1(b) + 2\sigma_2^2(b) = 0$. Indeed, in the case of a double inelastic collision, the triggered particle can be emitted in either of them – hence an extra factor 2. We see, in this way that the different contributions to $d\sigma/dy$ of a double scattering diagram cancel. It is easy to see that this cancellation is valid order by order in the total number of collisions. This can also be seen as follows. The total inelastic cross-section for pA collision in the Glauber model is given by the well known expression¹

$$\sigma_{inel}^{pA}(b) = \sum_{n=1}^A \sigma_n(b) = 1 - (1 - \sigma_{inel} T_A(b))^A . \quad (9)$$

This expression contains a term in A^1 (single-scattering or Born term). It also contains contribution from multiple scattering with alternate signs (shadowing corrections). Numerically, it behaves as A^α with $\alpha \sim 2/3$. The single particle inclusive cross-section is given by

$$\frac{d\sigma^{pA}}{dy}(b) \propto \sum_{n=1}^A n \sigma_n(b) = A \sigma_{inel} T_A(b) . \quad (10)$$

¹In the literature, the optical limit expression is often used instead of Eq. (8), namely

$$\sigma_n(b) = (\sigma_{inel} A T_A(b))^n \exp(-\sigma_{inel} A T_A(b)) / n! .$$

In this case we get $\sigma_{inel}^{pA}(b) = 1 - \exp(-\sigma_{inel} A T_A(b))$, which coincides with Eq. (9) in the large A limit. The same type of expressions are obtained in the eikonal model, since, in this case, the number of rescatterings is infinite.

We see that here multiple-scattering contributions cancel identically and only the Born term is left (impulse approximation). As a consequence of this cancellation the A -dependence of $d\sigma/dy$ in pA interactions behaves as A^1 . In the case of AB collisions it behaves as AB and $dN^{AB}/dy = (1/\sigma_{AB})d\sigma^{AB}/dy$ is proportional to $A^{4/3}$, i.e. to the number of binary collisions – rather than to the number of participants, as one would naively expect (see Section 3.2).

2.3 Shadowing Corrections in the Inclusive Cross-Section

The interest of this way of looking at the Glauber model resides in the fact that, as discussed in Section 2.2, it provides strict relations between contributions to the total cross-section and contributions to various inelastic processes of multiparticle production, which make up the total cross-section via unitarity. These relations are the so-called Abramovsky-Gribov-Kancheli (AGK) cutting rules [13], and have a general validity in RFT. The absence of shadowing corrections in the inclusive cross-section, Eq. (10), is called the AGK cancellation. As mentioned above, in the eikonal and Glauber models only the initial state is present in the vertex function (blob). Thus a secondary can only be produced in an interaction and the AGK cancellation is exact. In a general theory with a more complicated vertex function, the triggered particle can be produced in the blob. This gives rise to a violation of the AGK cancellation – which is responsible for the shadowing corrections to the inclusive spectra. Indeed, if the measured particle (trigger) is produced in the vertex function of a double scattering diagram, the extra factor 2 in $\sigma_2^2(b)$ is not present and the AGK cancellation is not valid. In this case the shadowing corrections in the inclusive cross-section are the same as in the total cross-section. This is the physical origin of the AGK violations present in the microscopic model described in Section 3. It is clear that if the blob has a small extension in rapidity, production from the blob will mainly contribute to the fragmentation region. Therefore, at mid-rapidities, and large energy, the AGK cancellation will be valid.

Let us consider next the contribution to the total cross-section resulting from the diffractive production of large mass states. Clearly, this is equivalent to an increase of the rapidity extension of the blob – which, in this case, can cover the mid-rapidity region. Therefore, shadowing corrections to the single particle inclusive cross-section can be present, at mid-rapidities, provided the measured particle is part of the diffractively produced system. We see in this way that shadowing corrections to $d\sigma/dy$ are related to diffractive production of large mass systems. The theoretical expression of the diffractive cross-section is well-known. It has also been measured experimentally and, thus, the shadowing corrections can be computed with no free parameters. In these lectures I will not elaborate any further on this last point. More details, as well as numerical calculations, can be found in [14].

2.4 Space-Time Development of the Interaction : Absence of Intra-Nuclear Cascade

The reggeon calculus or reggeon field theory (RFT) [11] provides the field theoretical formulation of the eikonal (for hh collisions) or the Glauber (for hA and AB) models, valid at high energies. The main difference between the RFT and the Glauber model is that, at high energies, the coherence length is large and the whole nucleus is involved in the interaction. Moreover, due to the space-time development of the interaction, when, at high energy, a projectile interacts inelastically with a nucleon of the nucleus, the formation time of (most of) the produced particles is larger than the nuclear size and, thus, most particles are produced outside the nucleus. Only slow particles in the lab reference frame are produced inside the nucleus and can interact with the nucleons of the nucleus they meet in their path (intra-nuclear cascade). At high energies, most of the produced particles have left the nucleus at the time they are formed. This near absence of nuclear cascade is well known experimentally. Actually, it constituted for a long time one of the main puzzles of high energy hadron-nuclear interactions.

Another consequence of the space-time development of the interaction, is that planar multiple-scattering diagrams give a vanishing contribution to the total cross-section at high energies. Indeed, as discussed above, the formation time of the multiparticle state is larger than the nuclear size and, therefore, there is no time for its rescattering with other nucleons of the nucleus. The relevant multiple scattering diagrams are non-planar ones, describing the “parallel” interactions of different constituents of the projectile with the target nucleons (in the case of an hA collision). This picture is in clear contrast with the Glauber model, in which the projectile undergoes successive (billiard ball type of) collisions with the nucleons of the target.

In spite of these differences, one recovers the Glauber formula in first approximation. As discussed above, this formula corresponds to the contribution of the initial state (on-shell projectile pole) to the various rescattering terms. In RFT one has, besides these contributions, also the contributions due to low mass and high mass diffractive excitations of the projectile. The latter are very important since, as we have seen in Section 2.3, they give rise to shadowing corrections to the inclusive cross-section.

2.5 Regge Poles : The Pomeron

Regge poles [15] [16] play an important role in high-energy interactions. It is important to give some basic concepts on Regge poles. Indeed, they provide a theoretical basis for the parametrization of the Born term in multiple-scattering models. More precisely, they give an important connection between high-energy behaviour and the spectrum of resonances in the t -channel. Also, it is very important for our purpose

in these lectures that they allow to determine, to a large extent, the momentum distribution functions of partons in hadrons, as well as their fragmentation functions. These are the main ingredients of the microscopic models introduced in the next section.

At high energies the exchange of a particle of spin J and mass M_J in the t -channel of a two-body amplitude $1 + 2 \rightarrow 3 + 4$ has the form

$$T(s, t) = g_{13} g_{24} s^J / (M_J^2 - t) . \quad (11)$$

When J is large ($J > 1$), the cross-section increases as a power s^{J-1} and violates the Froissart bound. This problem provided one of the main motivations for the introduction of Regge poles. Note that Eq. (11) is valid only close to the pole, i.e. for $t \sim M_J^2$. However, the physical values of t for the s -channel amplitude $1 + 2 \rightarrow 3 + 4$ are $t \lesssim 0$. In the Regge pole model, the behaviour (11) is modified for physical values of t , as follows

$$T(s, t) = g_{13}(t) g_{24}(t) s^{\alpha(t)} \eta(\alpha(t)) . \quad (12)$$

Here $g(t)$ are called Regge residues and $\alpha(t)$ is a function, called Regge trajectory, such that $\alpha(t = M_J^2) = J$. Thus, if $\alpha(t) \leq 1$ for physical values of t , the Froissard bound will be satisfied, irrespective of the value of J . For practical purposes one proceeds as follows. Let us consider the existing particles and/or resonances with the conserved quantum numbers (isospin, parity etc) of the t -channel. For each of them, let us plot its spin versus its mass (see Fig. 4). This is the so-called Chew-Frautschi plot [16]. (Actually, in a relativistic theory it is necessary to consider separately even and odd values of spin). It turns out that a large family of resonances, including ρ , ω , f and A_2 lie practically in a single straight line $\alpha_R(t) = \alpha_R(0) + \alpha' t$. Other resonances as K^* and ϕ lie on parallel Regge trajectories with $\alpha(t) < \alpha_R(t)$. Extrapolating to the physical region $t \leq 0$ one finds an intercept $\alpha_R(0) \sim 1/2$ and a slope $\alpha'_R \sim 0.9 \text{ GeV}^{-2}$. Since $\alpha_R(t) \lesssim 1/2$ for $t \lesssim 0$, the Froissard bound is respected. The function $\eta(\alpha(t)) = -[1 + \sigma \exp(-i\pi\alpha(t))]/\sin \pi\alpha(t)$ with $\sigma = +1$ (-1) for J even (odd). σ is called the signature : positive (negative) for $\sigma = +1$ (-1). Note that for a trajectory of positive (negative) signature, the numerator of η cancels the poles in the denominator corresponding to odd (even) values of spin. Note also that $\eta(\alpha(t))$ determines the phase of the amplitude in terms of $\alpha(t)$. In this way the phase of the amplitude is related to its high energy behaviour – also determined by $\alpha(t)$. (The validity of this relationship is much more general than the Regge pole model).

The Regge pole model has many features that have been tested by experiment (and no contradiction with experiment has been found). Among its successes is the factorization of Regge residues, Eq. (12). Another success is that, for any given two body process, when resonances exist in its t -channel, a (shrinking) peak is found in

the s -channel amplitude near $t = 0$ – as obtained from Eq. (12)². On the contrary, if the t -channel is “exotic” (i.e. no known resonance exists having its quantum numbers), the forward peak in the s -channel is absent. There is no exception to this rule.

Unfortunately, there is an important caveat. All Regge trajectories corresponding to known resonances have an intercept $\alpha(0) < 1$. Therefore, it is not possible to explain the increase with energy observed in total cross-sections. In order to do so, it is necessary to postulate the existence of a Regge pole with vacuum quantum numbers (so that it can be exchanged in all elastic amplitudes) and intercept larger than one. It is called the Pomeron and is believed to correspond to the exchange of glue-balls in the t -channel. To compute its trajectory in QCD is a very difficult task. Both non-perturbative and perturbative methods give indications that its trajectory is slightly above one ($\alpha_P(0) \sim 1.1 \div 1.3$) as required by experiment. In this way it is possible to explain the increase with energy of total cross-sections, i.e. $\sigma_{tot} \propto s^\Delta$ with $\Delta = \alpha_P(0) - 1 > 0$.

Note that for $\alpha_P(0) = 1$, the amplitude at $t = 0$ is purely imaginary. With $\alpha_P(0)$ slightly above unity the ratio of real to imaginary parts is small. Unfortunately, there is still a caveat. Since $\Delta = \alpha_P(0) - 1 > 0$, the Pomeron exchange again violates the Froissard bound. (This violation was one of the main motivations for Regge models, as discussed at the beginning of this subsection). The only way out is to use the Pomeron contribution as a Born term in a unitarization scheme – such as the eikonal or Glauber models discussed above. Indeed, if the contribution of the Born term or Pomeron (Fig. 1a) to σ_{tot} behaves as s^Δ , the sum of the series (Figs. 1b and 1c) behaves as $s^{\Delta'}$ with $\Delta' < \Delta$. Moreover, in the limit $s \rightarrow \infty$ the power behaviour of the Born term is converted into $(\ell n s)^2$, i.e. the maximal energy growth allowed by the Froissard bound³.

Technically, Regge poles are isolated poles in the complex angular momentum plane. Their s -channel iteration (as in the eikonal model) gives rise to cuts in this plane (Regge cuts). The latter violate factorization. However, it turns out that the sum of all eikonal diagrams is approximately factorizable.

²Assuming an exponential t -dependence for $g(t)$, we obtain from Eqs. (7) and (12), $T(s, t) \propto \exp[(2B + \alpha' \ell n s)t]$. We see that the forward peak has a width that increases logarithmically with increasing energy. This is called the shrinking of the forward peak and has been observed experimentally. In this way $r \propto \ell n s$, i.e. the effective radius of the hadron increases like $\ell n s$ as $s \rightarrow \infty$

³This can be seen as follows. If the cross-section of the Born term tends to infinity, the inelastic cross-section of the eikonal sum, at fixed b , tends to 1 (see footnote 1). Upon integration in b one obtains a geometrical cross-section, proportional to $r^2 \propto (\ell n s)^2$ (see footnote 2).

3 Microscopic String Models

3.1 Hadron-Hadron Interactions

The Dual Parton Model (DPM) [7] [8] and the Quark Gluon String Model (QGSM) [9] [10] are closely related dynamical models of soft hadronic interactions. They are based on the large- N expansion of non-perturbative QCD⁴ and on Gribov's Reggeon Field Theory (RFT) [11]. Their main aim is to determine the mechanism of multiparticle production in hadronic and nuclear interactions. The basic mechanism is well known in e^+e^- annihilation (Fig. 5). Here the e^+e^- converts into a virtual photon, which decays into a $q\bar{q}$ pair. In the rest system of the virtual photon the quark (colour 3) and the antiquark (colour $\bar{3}$) separate from each other producing one string (or chain) of hadrons, i.e. two back-to-back jets. Processes of this type are called one-string processes.

In hadron-hadron interactions, a one-string mechanism is also possible but only in some cases, namely when the projectile contains an antiquark (quark) of the same type than a quark (antiquark) of the target, which can annihilate with each other in their interaction. For instance in π^+p , the \bar{d} of π^+ can annihilate with the d of p and a single string is stretched between the u of π^+ (colour 3) and a diquark uu of p (colour $\bar{3}$). This mechanism is also possible in $\bar{p}p$ interactions (Fig. 6) but not in pp . This already indicates that it cannot give the dominant contribution at high energy. Indeed, when taking the square of the diagram of Fig. 6 (in the sense of unitarity) we obtain a planar graph, which is the dominant one according to the large- N expansion. However, this only means that this graph has the strongest coupling. Since flavour quantum numbers are exchanged between projectile and target, this graph gives a contribution to the total cross-section that decreases as an inverse power of s ($1/\sqrt{s}$). A decrease with s is always associated with flavor exchange. For instance, the charge exchange $\pi^-p \rightarrow \pi^0n$ cross-section also decreases as $1/\sqrt{s}$. As we have discussed in Section 2.5, only an exchange in the t -channel with vacuum quantum numbers (Pomeron), gives a contribution to σ_{tot} which does not vanish asymptotically. Actually, the diagram in Fig. 6 corresponds to the exchange of a Reggeon, with intercept $\alpha_R(0) \sim 1/2$.

In order to prevent the exchange of flavour between projectile and target, the \bar{d} and d have to stay, respectively, in the projectile and target hemispheres. Since they are coloured, they must hadronize stretching a second string of type $\bar{d}-d$. We obtain in this way a two-string diagram (Figs. 7-9)). Taking the square of this diagram, we obtain a graph with the topology of a cylinder (Fig. 10). It turns out that this

⁴The Feynman graphs of a gauge field theory with N degrees of freedom can be classified according to their topology. The graphs with the simplest topology are dominant. The contribution of graphs with more complicated topology (characterized by well defined topological indices) are suppressed by powers of $1/N$ [17-19].

is the simplest topology one can construct which does not vanish as $s \rightarrow \infty$ due to flavour exchange. Therefore, we obtain in this way the dominant graph for hadron-hadron scattering at high energy. The diagram in Fig. 10 corresponds to a Pomeron (P) exchange and the graphs in Figs. 7-9 are called a cut Pomeron. Its order in the large- N expansion is $1/N^2$ [17-19]. Note that due to energy conservation the longitudinal momentum fractions taken by the two components at the string ends have to add up to unity.

There are also higher order diagrams (in the sense of the large- N expansion) with 4, 6, 8 strings which give non-vanishing contributions at high energy. An example of the next-to-leading graph for pp interactions is shown in Fig. 9. It contains four strings – the two extra strings are stretched between sea quarks and antiquarks. The square of this graph corresponds [20] to a two Pomeron exchange (Fig. 1b) and has the topology of a cylinder with a handle. Its order in the large- N expansion is $1/N^4$. The one with six strings corresponds [20] to a three Pomeron exchange (Fig. 1c) and to the topology of a cylinder with two handles (order $1/N^6$), etc.

In this way, the large- N expansion provides the microscopic (partonic) description of the Reggeon and Pomeron exchanges and of their s -channel iterations (Figs. 3), which were discussed in Section 2 in a hadronic picture.

The single particle inclusive spectrum is then given by [7]

$$\begin{aligned} \frac{dN^{pp}}{dy}(y) &= \frac{1}{\sum_n \sigma_n} \sum_n \sigma_n \left(N_n^{qq-qv}(y) + N_n^{qv-qq}(y) + (2n-2)N_n^{qs-\bar{q}s}(y) \right) \\ &\simeq N_k^{qq-qv}(y) + N_k^{qv-qq}(y) + (2k-2)N_k^{qs-\bar{q}s}(y) \end{aligned} \quad (13)$$

where $k = \sum_n n\sigma_n / \sum_n \sigma_n$ is the average number of inelastic collisions. Note that each term consists of $2n$ strings, i.e. two strings per inelastic collisions. Two of these strings, of type $qq-q$, contain the diquarks of the colliding protons. All other strings are of type $q-\bar{q}$.

The weights σ_n of the different graphs, i.e. their contribution to the total cross-section, cannot be computed in the large- N expansion. However, as discussed above there is a one-to-one correspondence [20] between the graphs in the large- N expansion and those in a multiple scattering model (Figs. 1). Thus, we use the weights obtained from the latter – with the parameters determined from a fit to total and elastic cross-sections (see Section 2). At SPS energies we get $k = 1.4$ and at RHIC $k = 2$ at $\sqrt{s} = 130$ GeV and $k = 2.2$ at $\sqrt{s} = 200$ GeV [21].

The hadronic spectra of the individual strings $N(y)$ are obtained from convolutions of momentum distribution functions, giving the probability to find a given constituent (valence quark, sea quark or diquark) in the projectile or in the target, with the corresponding fragmentation functions. Let us consider, for instance, one of the two $qq-q$ strings in Fig. 9. As shown in this figure, the total energy \sqrt{s} in the

pp center of mass frame (CM) is shared between the two strings. If $\sqrt{s_{str}}$ denotes the invariant mass of a string, we have $s_{str} = sx_2(1 - x_1)$ where $1 - x_1 = x_+$ and $x_2 = x_-$ are the light-cone momentum fractions of the constituents at the string ends, qq and q , respectively. For massless quarks, the rapidity shift between the pp CM and the CM of the string is $\Delta = 1/2 \log(x_+/x_-)$. We then have

$$N_1^{qq-q}(s, y) = \int_0^1 \int_0^1 dx_+ dx_- \rho_1^{qq}(x_+) \rho_1^q(x_-) \frac{dN^{qq-q}}{dy}(y - \Delta; s_{str}) . \quad (14)$$

The subscript 1 in N and ρ indicates that there is only one interaction (two strings). The momentum distribution functions ρ give the probability to find a quark or diquark in the proton carrying a given momentum fraction. dN^{qq-q}/dy is the rapidity distribution of hadron h in the CM of the $qq-q$ string obtained from q and qq fragmentation functions :

$$\frac{dN^{qq-q}(y - \Delta; s_{str})}{dy} = \begin{cases} \bar{x}_h D_{qq \rightarrow h}(x_h) & y \geq \Delta , \\ \bar{x}_h D_{q \rightarrow h}(x_h) & y < \Delta , \end{cases} \quad (15)$$

where

$$x_h = |2\mu_h \sinh(y - \Delta)/\sqrt{s_{str}}| , \quad \bar{x}_h = \left(x_h^2 + 4\mu_h^2/s_{str}\right)^{1/2} . \quad (16)$$

μ_h is the transverse mass of the detected particle h , and $D_{q \rightarrow h}$ and $D_{qq \rightarrow h}$ are the quark and diquark fragmentation functions. Momentum distribution and fragmentation functions can be obtained from Regge intercepts. Let us discuss first the former. In order to determine the behaviour near $x = 0$ of the momentum distribution of a quark in a proton, it is convenient to look at the diagram in Fig. 6. As discussed in Section 2.5, the square of this diagram (in the sense of unitarity) gives a contribution to the total cross-section $s^{\alpha_R(0)-1} = e^{\Delta y(1-\alpha_R(0))}$ where $\Delta y = y - y_{max}$. Here y is the quark rapidity and y_{max} its maximal value. Recalling that $dy = dx/x$, we obtain $\rho_p^q(x_q) \propto x_q^{-\alpha_R(0)} = 1/\sqrt{x_q}$ as $x_q \rightarrow 0$. In order to determine its behaviour as $x_q \rightarrow 1$, we have to use the momentum conservation $x_q + x_{qq} = 1$ (see Fig. 9). Thus, in order to have $x_q \rightarrow 1$ it is necessary that $x_{qq} \rightarrow 0$. The corresponding Regge exchange in the t -channel consists of two quarks and two antiquarks. Such a state is called a baryonium and the corresponding Regge intercept is known experimentally to be -1.5 ± 0.5 . Taking the product of $x \rightarrow 0$ and $x \rightarrow 1$ behaviours we obtain

$$\rho_1^q(x_q) = \rho_1^{qq}(x_{qq}) = C x_q^{-1/2} x_{qq}^{1.5} \delta(1 - x_q - x_{qq}) = C \frac{1}{\sqrt{x_q}} (1 - x_q)^{1.5} \quad (17)$$

C is a constant determined from the normalization to unity. We see from Eq. (17) that, in average, the quark is slow and the diquark fast.

In order to generalize Eq. (17) to the case of n inelastic interactions ($2n$ strings), we just take the product of factors giving the $x \rightarrow 0$ behaviour of each constituent, times a δ -function of momentum conservation. The momentum distribution function $\rho_n(x)$ of each individual constituent is then obtained by integrating over the x -values of the other $2n - 1$ constituents⁵. In this way the behaviour $x \rightarrow 0$ is unchanged, whereas the power of $1 - x$ increases with n , due to momentum conservation. Indeed, the average momentum fraction taken by each constituent decreases when the number of produced strings increases. Obviously in the case of n inelastic collisions Eq. (14) is still valid with ρ_1 replaced by ρ_n . All details can be found in [7] [9].

The same Regge model considerations allow to determine the $x_h \rightarrow 1$ behaviour of the fragmentation functions. Writing

$$\bar{x}_h D_{i \rightarrow h}(x_h) \propto (1 - x_h)^{\beta_i^h} \quad (18)$$

for the fragmentation function of constituent i into hadron h (see Eq. (15)), one finds [22] $\beta_i^h = -\alpha_{k\bar{k}}(0) + \lambda$ where $\alpha_{k\bar{k}}(0)$ is the intercept of the $(k\bar{k})$ Regge trajectory, k is the system of leftover (spectator) constituents and λ is a constant resulting from transverse momentum integrations and estimated to be $\lambda \sim \frac{1}{2}$ [22]. For example, for the fragmentation $u \rightarrow \pi^+$, the system k is a d -quark and $\beta_u^{\pi^+} = -\alpha_{d\bar{d}}(0) + \lambda$. Likewise, for the fragmentation of a ud diquark into a proton we have $\beta_{ud}^p = -\alpha_{u\bar{u}}(0) + \lambda$ and for that of a ud diquark into Λ , $\beta_{ud}^\Lambda = -\alpha_{s\bar{s}}(0) + \lambda$. Here $\alpha_{u\bar{u}}(0) = \alpha_{d\bar{d}}(0) = \alpha_R(0) = 1/2$ and $\alpha_{s\bar{s}}(0) = \alpha_\phi(0) = 0$. This gives a different behaviour of the p and Λ inclusive spectrum which is observed experimentally.

Note that in writing Eq. (13) we have assumed that individual strings are independent from each other. In this way, the hadronic spectra of a given graph are obtained by adding up the corresponding ones for the individual strings. This leads to a picture, in which, for any individual graph, particles are produced with only short-range (in rapidity) correlations. Long-range correlations (and a broadening of the multiplicity distributions) are due to fluctuations in the number of strings, i.e. to the superposition of different graphs with their corresponding weights. This gives a simple and successful description of the data in hadron-hadron and hadron-nucleus interactions [7-10].

3.2 Nucleus-Nucleus Interactions

The generalization of Eq. (3) to nucleus-nucleus collisions is rather straightforward. For simplicity let us consider the case of AA collisions and let n_A and n be the

⁵Taking the same $1/\sqrt{x}$ behaviour for both valence and sea quarks [9] [10], these integrals can be performed analytically and one gets : $\rho_n^q(x) = C_n x^{-1/2} (1-x)^{n+1/2}$ and $\rho_n^{qq}(x) = C'_n x^{1.5} (1-x)^{n-3/2}$, with $C_n = \Gamma(n+2)/\Gamma(1/2)\Gamma(n+3/2)$ and $C'_n = \Gamma(n+2)/\Gamma(5/2)\Gamma(n-1/2)$.

average number of participants of each nucleus and the average number of binary NN collisions, respectively⁶. At fixed impact parameter b , we have [23] [7]

$$\begin{aligned} \frac{dN^{AA}}{dy}(b) = n_A(b) & \left[N_{\mu(b)}^{qq-qv}(y) + N_{\mu(b)}^{qv-qq}(y) + (2k-2)N_{\mu(b)}^{qs-\bar{q}s}(y) \right] \\ & + (n(b) - n_A(b)) 2k N_{\mu(b)}^{qs-\bar{q}s}(y) . \end{aligned} \quad (19)$$

The physical meaning of Eq. (19) is quite obvious. The expression in brackets corresponds to a NN collision. Since n_A nucleons of each nucleus participate in the collision, this expression has to be multiplied by n_A . Note that in Eq. (13) the average number of collisions is k – and the number of strings $2k$. In the present case the total average number of collisions is kn – and the number of strings $2kn$. The second term in Eq. (2) is precisely needed in order to have the total number of strings required by the model. Note that there are $2n_A$ strings involving the valence quarks and diquarks of the participating nucleons. The remaining strings are necessarily stretched between sea quarks and antiquarks. The value of $\mu(b)$ is given by $\mu(b) = k\nu(b)$ with $\nu(b) = n(b)/n_A(b)$, $\mu(b)$ represents the total average number of inelastic collisions suffered by each nucleon. Actually, Eq. (19) is an approximate expression, involving the same approximation as in Eq. (13). The exact expression can be found in [23] [7].

We see from Eq. (19) that dN^{AA}/dy is obtained as a linear combination of the average number of participants and of binary collisions. The coefficients are determined within the model and depend on the impact parameter via $\mu(b)$. As discussed in Section 3.1 the average invariant mass of a string containing a diquark at one end is larger than the one of a $q\bar{q}$ string since the average momentum fraction taken by a diquark is larger than that of quark. It turns out that the same is true for the central plateau, i.e. : $N^{qq-q}(y^* \sim 0) > N^{q-\bar{q}}(y^* \sim 0)$. Let us now consider two limiting cases :

$$\text{If } N^{qs-\bar{q}s}(y^* \sim 0) \ll N^{qq-qv}(y^* \sim 0) , \text{ then } \frac{dN^{AA}}{dy}(y^* \sim 0) \sim n_A \sim A^1 \quad (20)$$

$$\text{If } N^{qs-\bar{q}s}(y^* \sim 0) \sim N^{qq-qv}(y^* \sim 0) , \text{ then } \frac{dN^{AA}}{dy}(y^* \sim 0) \sim n \sim A^{4/3} . \quad (21)$$

⁶ $n_A(b) = \int d^2s AT_A(s) [1 - \exp(-\sigma_{pp} AT_A(b-s))] / \sigma_{AA}(b)$ and $n(b) = \sigma_{pp} \int d^2s A^2 T_A(s) T_A(b-s) / \sigma_{AA}(b) = \sigma_{pp} A^2 T_{AA}(b) / \sigma_{AA}(b)$. These expressions can be obtained in the Glauber model as follows. One has to generalize Eq. (8) to the case of AB collisions. The corresponding cross-sections $\sigma_{n_A, n_B, n}(b)$ depend on three indices : $n_A(n_B)$ is the number of participants of nucleus $A(B)$ and n is the number of NN collisions. Then, $n_A(b) = \sum_{n_A, n_B, n} n_A \sigma_{n_A, n_B, n}(b) / \sum_{n_A, n_B, n} \sigma_{n_A, n_B, n}(b)$ and $n(b) = \sum_{n_A, n_B, n} n \sigma_{n_A, n_B, n}(b) / \sum_{n_A, n_B, n} \sigma_{n_A, n_B, n}(b)$.

In the first case we obtain a proportionality in the number of participants n_A whereas in the second case we obtain a proportionality in the number of binary collisions. Since $dN^{AA}/dy \equiv (1/\sigma_{AA})d\sigma^{AA}/dy$, the latter result implies that $d\sigma^{AA}/dy \sim A^2$, i.e. all unitarity corrections cancel and we obtain the same result as in the impulse approximation (Born term only). This result is the AGK cancellation discussed in Section 2. It implies that, for the inclusive cross-section, soft and hard processes have the same A -dependence. However, as discussed in Section 2 the AGK cancellation is violated by diagrams related to the diffraction production of large-mass states. These diagrams give rise to shadowing corrections. Their effect is very important in nuclear collisions since they are enhanced by $A^{1/3}$ factors.

3.3 Charged Particle Multiplicities

At SPS energies the limit given by Eq. (21) is not reached, and Eq. (19) leads to an A dependence of dN^{AA}/dy at $y^* \sim 0$ in A^α with α only slightly above unity. ($\alpha \sim 1.08$ between 2 and 370 participants). On the other hand, shadowing corrections are small due to phase space limitations. The results [21] for $Pb Pb$ collisions at $\sqrt{s} = 17.3$ GeV are shown in Fig. 10. We see that both the absolute values and the centrality dependence are well reproduced. When the energy increases, Eq. (21) shows that the value of α should increase towards $4/3$, in the absence of shadowing corrections. However, the effect of the latter is increasingly important and, as a result, the value of α varies little with s . At $\sqrt{s} = 130$ GeV, without shadowing corrections the A -dependence is A^α , with $\alpha \sim 1.27$ in the same range of n_{part} – a value which is not far from the maximal one, $\alpha = 4/3$ from Eq. (21). With the shadowing corrections taken into account, the A -dependence is much weaker (lower line of the shaded area in Fig. 11) [21]. The A -dependence is now A^α with $\alpha \sim 1.13$ – always in the range of n_{part} from 2 to 370. As we see, the increase of α from SPS to RHIC energies is rather small. This value of α is predicted to change very little between RHIC and LHC, where $\alpha \approx 1.1$. For, the increase from $\alpha \sim 1.27$ to $\alpha \sim 4/3$ obtained in the absence of shadowing is compensated by an increase in the strength of the shadowing corrections, leaving the effective value of α practically unchanged. This implies that dN/dy at $y^* \sim 0$ in central $Au Au$ collisions will increase by a factor $2 \div 2.5$ between RHIC and LHC. This increase is slightly smaller than the corresponding increase of $d\sigma/dy$ in pp collisions.

4 Nuclear Stopping

In pp collisions the net proton ($p-\bar{p}$) distribution is large in the fragmentation regions and has a deep minimum at mid-rapidities. In contrast to this situation a much flatter distribution has been observed [24] in central $Pb Pb$ collisions at CERN-SPS.

In view of that, several authors have claimed that the stopping in heavy ion collisions is anomalous, in the sense that it cannot be reproduced with the same mechanism (and the same values of the parameters) used to describe the pp data. In a recent paper [25] it has been shown that this claim is not correct.

In the model described in the previous section, the net baryon can be produced directly from the fragmentation of the diquark. Another possibility is that the diquark splits producing a leading meson in the first string break-up and the net baryon is produced in a further break-up. Clearly, in the first case, the net baryon distribution will be more concentrated in the fragmentation region than in the second case. The corresponding rapidity distributions are related to the intercepts of the relevant Regge trajectories, α_{qq} and α_q , respectively, i.e. they are given by $e^{\Delta y(1-\alpha)}$ (see Section 3.1). Here Δy is the difference between the rapidity of the produced net baryon and the maximal one. In the case of the first component, in order to slow down the net baryon it is necessary to slow down a diquark. The corresponding Regge trajectory is called baryonium and its intercept is known experimentally to be $\alpha_{qq} \equiv \alpha_{qq\bar{q}\bar{q}}(0) = -1.5 \pm 0.5$ (see Section 3.1). For the second component, where a valence quark is slowed down, we take $\alpha_q \equiv \alpha_{q\bar{q}}(0) = \alpha_R(0) = 1/2$ ⁷.

In this way we arrive to the following two component model for net baryon production $B_i - \bar{B}_i$ (where i denotes the baryon species) out of a single nucleon

$$\begin{aligned} \frac{dN^{B_i - \bar{B}_i}}{dy}(y, b) = & I_2^i a C_{\mu(b)} Z_+^{1-\alpha_q(0)} (1 - Z_+)^{\mu(b)-3/2+n_{sq}(\alpha_R(0)-\alpha_\phi(0))} \\ & + I_1^i (1 - a) C'_{\mu(b)} Z_+^{1-\alpha_{qq}(0)} \times (1 - Z_+)^{\mu(b)-3/2+c+n_{sq}(\alpha_R(0)-\alpha_\phi(0))} \end{aligned} \quad (22)$$

where n_{sq} is the number of strange quarks in the hyperon, $\alpha_R(0) = 1/2$, $\alpha_\phi(0) = 0$, $Z_+ = (e^{y-y_{max}})$, y_{max} is the maximal value of the baryon rapidity and $\mu(b)$ is the average number of inelastic collisions suffered by the nucleon at fixed impact parameter b (see Section 3.2). The constants C_μ and C'_μ are normalization constants required by baryon number conservation⁸. The small Z behaviour is controlled by the corresponding intercept. The factor $(1 - Z_+)^{\mu(b)-3/2}$ gives the $Z \rightarrow 1$ behaviour of the diquark momentum distribution function in the case of μ inelastic collisions (see footnote 5). Following conventional Regge rules an extra $\alpha_R(0) - \alpha_\phi(0) = 1/2$ is added to the power of $1 - Z_+$ for each strange quark in the hyperon (see Section 3.1, Eq. (18)).

⁷There is a third possibility in which the net-baryon transfer in rapidity takes place without valence quarks (string junction or gluonic mechanism) with intercept either $\alpha_{SJ} = 1/2$ [26] or $\alpha_{SJ} = 1$ [27]. We find no evidence for such a component from the existing pp and AA data. Its smallness could be related to the fact that it produces an extra string of hadrons and, thus, does not correspond to the dominant topology in the large N expansion.

⁸ $C_\nu = \Gamma(a + b)/\Gamma(a)\Gamma(b)$ with $a = 1 - \alpha_q(0)$ and $b = \mu(b) - 1/2 + n_{sq}(\alpha_R(0) - \alpha_\phi(0))$; $C'_\nu = \Gamma(a' + b')/\Gamma(a')\Gamma(b')$ with $a' = 1 - \alpha_{qq}(0)$ and $b' = \mu(b) - 1/2 + c + n_{sq}(\alpha_R(0) - \alpha_\phi(0))$.

The weights I_2^i and I_1^i allow to determine the relative yields of the different baryon and antibaryon species. They are computed in Appendix A using simple quark counting rules.

The fraction, a , of the first component is treated as a free parameter. The same for the parameter c in the second component – which has to be determined from the shape of the (non-diffractive) proton inclusive cross-section in the baryon fragmentation region. It can be seen from Eq. (22) that stopping increases with $\mu(b)$, i.e. with the total number of inelastic collisions suffered by each nucleon. This effect is present in the two terms of (22) and is a consequence of energy conservation. The question is whether this “normal” stopping is sufficient to reproduce the data. In other words whether the data can be described with a universal value of a , i.e. independent of μ and the same for all reactions.

The formulae to compute net baryon production in pp or AA collisions can be obtained from Eq. (22) in a straightforward way. Thus, in AA collisions we have : $dN^{AA \rightarrow B_i - \bar{B}_i} / dy(y^*, b) = n_A(b)[dN^{B_i - \bar{B}_i} / dy(y^*, b) + dN^{B_i - \bar{B}_i} / dy(-y^*, b)]$.

Note that in the formalism above, baryon quantum number is exactly conserved. Note also that shadowing corrections are not present. Indeed, as explained in Section 2, these corrections affect only the term proportional to the number of binary collisions, which is not present for net baryon production.

A good description of the data on the rapidity distribution of $pp \rightarrow p - \bar{p} + X$ both at $\sqrt{s} = 17.2$ GeV and $\sqrt{s} = 27.4$ GeV is obtained from Eq. (22) with $a = 0.4$, $c = 1$, $\alpha_q = 1/2$ and $\alpha_{qq} = -1$. The results are shown in Table 1 at three different energies, and compared with the data. As we see the agreement is reasonable. As it is well known, a pronounced minimum is present at $y^* = 0$. There is also a substantial decrease of the mid-rapidity yields with increasing energy. Also, the mid-rapidity distributions get flatter with increasing energy since the net proton peaks are shifted towards the fragmentation regions.

It is now possible to compute the corresponding net baryon production in heavy ion collisions and to check whether the data can be described with Eq. (22) using the same set of parameters as in pp . The results for net protons ($p - \bar{p}$) in central $Pb Pb$ collisions at $\sqrt{s} = 17.2$ GeV and central $Au Au$ collisions at $\sqrt{s} = 200$ GeV are shown in Fig. 14. We see a dramatic change in the shape of the rapidity distribution between the two energies, which is reasonably described by the model. Therefore, we conclude that there is no need for a new mechanism in AA collisions.

5 Hyperon and Antihyperon Production

Strange particle production, in particular, of multistrange hyperons, has been proposed as a signal of Quark Gluon Plasma formation. Flavor equilibration is very efficient in a plasma due to large gluon densities and low thresholds [4]. Moreover,

the increase of the relative yields of strange particles in central AA collisions as compared to pp can be understood as a consequence of the necessity of using the canonical ensemble in small size systems (pp) – rather than the grand canonical one. The exact conservation of quantum numbers in the former leads to a reduction of $s\bar{s}$ pair production, as compared to the latter [5].

An analysis of the results at SPS in the framework of the present model has been presented in [28]. In the following we concentrate on RHIC results.

A general result in DPM is that the ratios B/h^- and \bar{B}/h^- of baryon and antibaryon yields over negatives decrease with increasing centralities. This is easy to see from Eq. (19). The production from $q_s\bar{q}_s$ strings scales with the number of binary collisions. These strings have a smaller (average) invariant mass than the $qq\bar{q}$ strings and, thus, are more affected by the thresholds needed for $B\bar{B}$ pair production. As a consequence, the centrality dependence of B and \bar{B} production will be smaller than the one of negatives. The effect is rather small at RHIC energies. However, it is sizable and increases with the mass of the produced baryon. In contrast with this situation, the data for Λ 's show no such decrease and an increase is present for Ξ production. Data on Ω production are not yet available. However, SPS data clearly show a hierarchy in the sense that the enhancement of baryon production increase with the mass (or strange quark content) of the produced baryon.

The only way out we have found is to give up the assumption of string independence. Until now we have assumed that particles produced in different strings are independent from each other. In the following we allow for some final state interactions between comoving hadrons or partons. We proceed as follows.

The hadronic densities obtained in Section 2 are used as initial conditions in the gain and loss differential equations which govern final state interactions. In the conventional derivation [29] of these equations, one uses cylindrical space-time variables and assumes boost invariance. Furthermore, one assumes that the dilution in time of the densities is only due to longitudinal motion, which leads to a τ^{-1} dependence on the longitudinal proper time τ . These equations can be written [29] [28]

$$\tau \frac{d\rho_i}{d\tau} = \sum_{k\ell} \sigma_{k\ell} \rho_k \rho_\ell - \sum_k \sigma_{ik} \rho_i \rho_k . \quad (23)$$

The first term in the r.h.s. of (23) describes the production (gain) of particles of type i resulting from the interaction of particles k and ℓ . The second term describes the loss of particles of type i due to its interactions with particles of type k . In Eq. (23) $\rho_i = dN_i/dyd^2s(y, b)$ are the particles yields per unit rapidity and per unit of transverse area, at fixed impact parameter. They can be obtained from the rapidity densities, Eq. (19), using the geometry, i.e. the s -dependence of n_A and n . The procedure is explained in detail in [30] where the pion fragmentation functions are also given. Those of kaons and baryons can be found in [31]. These fragmentation

functions are obtained using the procedure sketched at the end of Section 3.1 (see Eq. (18)). $\sigma_{k\ell}$ are the corresponding cross-sections averaged over the momentum distribution of the colliding particles.

Equations (23) have to be integrated from initial time τ_0 to freeze-out time τ_f . They are invariant under the change $\tau \rightarrow c\tau$ and, thus, the result depends only on the ratio τ_f/τ_0 . We use the inverse proportionality between proper time and densities and put $\tau_f/\tau_0 = (dN/dyd^2s(b))/\rho_f$. Here the numerator is given by the DPM particles densities. We take $\rho_f = [3/\pi R_p^2](dN^-/dy)_{y^*\sim 0} = 2 \text{ fm}^{-2}$, which corresponds to the density of charged and neutrals per unit rapidity in a pp collision at $\sqrt{s} = 130 \text{ GeV}$. This density is about 70 % larger than at SPS energies. Since the corresponding increase in the AA density is comparable, the average duration time of the interaction will be approximately the same at CERN SPS and RHIC – about 5 to 7 fm.

Next, we specify the channels that have been taken into account in our calculations. They are

$$\pi N \rightleftharpoons K\Lambda(\Sigma), \quad \pi\Lambda(\Sigma) \rightleftharpoons K\Xi, \quad \pi\Xi \rightleftharpoons K\Omega. \quad (24)$$

We have also taken into account the strangeness exchange reactions

$$\pi\Lambda(\Sigma) \rightleftharpoons KN, \quad \pi\Xi \rightleftharpoons K\Lambda(\Sigma), \quad \pi\Omega \rightleftharpoons K\Xi \quad (25)$$

as well as the channels corresponding to (24) and (25) for antiparticles. We have taken $\sigma_{ik} = \sigma = 0.2 \text{ mb}$, i.e. a single value for all reactions in (24) and (25) – the same value used in ref. [28] to describe the CERN SPS data.

Before discussing the numerical results and the comparison with experiment let us examine the qualitative effects of comovers interaction. As explained in the beginning of this Section, without final state interactions all ratios K/h^- , B/h^- and \bar{B}/h^- decrease with increasing centrality. The final state interactions (24), (25) lead to a gain of strange particle yields. The reason for this is the following. In the first direct reaction (24) we have $\rho_\pi > \rho_K$, $\rho_N > \rho_\Lambda$, $\rho_\pi\rho_N \gg \rho_K\rho_\Lambda$. The same is true for all direct reaction (24). In view of that, the effect of the inverse reactions (24) is small. On the contrary, in all reactions (25), the product of densities in the initial and final state are comparable and the direct and inverse reactions tend to compensate with each other. Baryons with the largest strange quark content, which find themselves at the end of the chain of direct reactions (24) and have the smallest yield before final state interaction, have the largest enhancement. Moreover, the gain in the yield of strange baryons is larger than the one of antibaryons since $\rho_B > \rho_{\bar{B}}$. Furthermore, the enhancement of all baryon species increases with centrality, since the gain, resulting from the first term in Eq. (23), contains a product of densities and thus, increases quadratically with increasing centrality.

In Fig. 15a-15d we show the rapidity densities of B , \bar{B} and $B - \bar{B}$ versus $h^- = dN^-/d\eta = (1/1.17)dN^-/dy$ [31] and compare them with available data [32-34]. We would like to stress that the results for Ξ and $\bar{\Xi}$ were given [31] before the data [34]. This is an important success of our approach.

In first approximation, the yields of p , \bar{p} , Λ and $\bar{\Lambda}$ yields over h^- are independent of centrality. Quantitatively, there is a slight decrease with centrality of p/h^- and \bar{p}/h^- ratios, a slight increase of Λ/h^- and $\bar{\Lambda}/h^-$ and a much larger increase for Ξ ($\bar{\Xi}$)/ h^- and Ω ($\bar{\Omega}$)/ h^- . This is better seen in Figs. 16a and 16b where we plot the yields of B and \bar{B} per participant normalized to the same ratio for peripheral collisions versus n_{part} . The enhancement of B and \bar{B} increases with the number of strange quarks in the baryon. This increase is comparable to the one found at SPS between pA and central $Pb Pb$ collisions. (In the statistical approach [5], the enhancement of B and \bar{B} relative to pp decreases with increasing energy. This may allow to distinguish between the two approaches).

The ratio K^-/π^- increases by 30 % in the same centrality range, between 0.11 and 0.14 in agreement with present data. The ratios \bar{B}/B have a mild decrease with centrality of about 15 % for all baryon species – which is also seen in the data. Our values for $N^{ch}/N_{max}^{ch} = 1/2$ are : $\bar{p}/p = 0.69$, $\bar{\Lambda}/\Lambda = 0.74$, $\bar{\Xi}/\Xi = 0.79$, $\Omega/\bar{\Omega} = .83$, to be compared with the measured values [35] :

$$\bar{p}/p = 0.63 \pm 0.02 \pm 0.06 \quad , \quad \bar{\Lambda}/\Lambda = 0.73 \pm 0.03 \quad , \quad \bar{\Xi}/\Xi = 0.83 \pm 0.03 \pm 0.05 \quad .$$

The ratio $K^+/K^- = 1.1$ and has a mild increase with centrality, a feature also seen in the data.

Note that a single parameter has been adjusted in order to determine the absolute yields of $B\bar{B}$ pair production, namely the \bar{p} one – which has been adjusted to the experimental \bar{p} value for peripheral collisions. The yields of all other $B\bar{B}$ pairs has been determined using the quark counting rules given in Appendix A.

Although the inverse slopes (“temperature”) have not been discussed here, let us note that in DPM they are approximately the same for all baryons and antibaryons both before and after final state interaction – the effect of final state interaction on these slopes being rather small [36].

6 J/ψ Suppression

A most interesting signature of the production of QGP is the suppression of resonance production [3]. As a consequence of deconfinement, the resonances are “melted”, i.e. the bound state cannot be formed. More precisely, as in the case of an ordinary plasma, the potential $V_0(r)$ is screened (Debye screening), i.e. it is changed into $V_0(r) \exp(-r/r_D(T))$. Here $r_D(T)$ is the Debye radius that decreases

with increasing temperature. When $r_D(T)$ becomes smaller than the hadronic radius, the bound state cannot be formed. This idea is particularly interesting in the case of the J/ψ (a resonance consisting of a charm quark and its antiquark). Indeed, it has been shown that the melting of the J/ψ occurs at temperature only slightly higher than the critical temperature at which QGP is formed. Moreover, the production of $c\bar{c}$ pairs is very rare. If they cannot bind together the $\bar{c}(c)$ will combine with a light quark (antiquark) giving rise to a $\bar{D}(D)$ meson (open charm)⁹.

The NA38-NA50 collaborations have observed a decrease of the ratio of J/ψ to dimuon (DY) cross-sections with increasing centrality in SU and $Pb Pb$ collisions [37]. The same phenomenon has been observed in pA collisions with increasing values of A . In this case, it is interpreted as due to the interaction of the pre-resonant $c\bar{c}$ pair with the nucleons of the nucleus it meets in its path (nuclear absorption). [Indeed, the formation time of the J/ψ is longer and it is produced outside the nucleus.] As a result of this interaction, the $c\bar{c}$ pair is modified in such a way that, after interaction, it has no projection into J/ψ (a $D\bar{D}$ pair is produced instead). The corresponding cross-section is denoted σ_{abs} (absorptive cross-section).

The survival probability, $S_{abs}(b)$, of the J/ψ in pA collisions can be easily calculated in the probabilistic Glauber model. One has

$$S_{abs}^A(b) = \frac{\int_{-\infty}^{+\infty} dZ \rho_A(b, Z) \left(1 - \sigma_{abs} \int_Z^{+\infty} \rho_A(b, Z_1) dZ_1\right)^{A-1}}{\int_{-\infty}^{+\infty} dZ \rho_A(b, Z)} = \frac{1}{\sigma_{abs} A T_A(b)} \{1 - [1 - \sigma_{abs} T_A(b)]\}^A . \quad (26)$$

Indeed, the $c\bar{c}$ pair is produced at a point of coordinates (b, Z) inside the nucleus, with probability proportional to $\rho_A(b, Z)$. The term inside the parenthesis gives the probability of non-absorption during its subsequent propagation through the nucleus. Note that $S_{abs} = 1$ for $\sigma_{abs} = 0$. The generalization of (26) to the case of nucleus-nucleus interactions is rather straightforward. We have [30]

$$S_{abs}^{AB}(b, s) = S_{abs}^A(s) S_{abs}^B(b - s) . \quad (27)$$

The NA50 collaboration has shown that the J/ψ suppression in $Pb Pb$ collisions has an anomalous component, i.e. it cannot be reproduced using nuclear absorption alone [37]. Two main interpretations have been proposed : deconfinement and comovers interaction. The latter mechanism has been described in Section 5 for hyperon production. In the case of J/ψ suppression, a single channel is important namely $c\bar{c}$ (or J/ψ) interacting with comoving hadrons and producing a $D\bar{D}$ pair. In this case, Eq. (23) can be solved analytically. One obtains for the expression of the survival probability S_{co} [30]

⁹In what follows we disregard the possibility of c and \bar{c} recombination into a J/ψ .

$$S_{co}^{AB}(b, s) = \exp \left[-\sigma_{co} \frac{3}{2} N_{yDT}^{co}(b, s) \ell n \frac{\tau_f}{\tau_0} \right]. \quad (28)$$

Here $N_{yDT}^{co}(b, s)$ is the density of charged particles in the rapidity region of the dimuon trigger (DT) ($0 < y^* < 1$) computed from Eq. (19). The factor $3/2$ takes care of the neutrals. For τ_f/τ_0 in Eq. (28) we use the expression given in Section 5, with $\rho_f = 1.15 \text{ fm}^{-2}$ at SPS energies. Note that S_{co} depends on a single parameter σ_{co} , the effective cross-section for comovers interaction.

The results [38] of the comovers interaction model are presented in Fig. 17. The agreement with the data [37] is quite satisfactory. There is a single free parameter $\sigma_{co} = 0.65 \text{ mb}$. The value of $\sigma_{abs} = 4.5 \text{ mb}$ is determined [38] from the pA data and the absolute normalization (47) from the SU ones.

Predictions of the comovers model [38] at RHIC energies are given in Figure 18.

In a deconfining approach one proceeds as follows [39]. One assumes that the energy density of the produced system is proportional to the density of participants $n_A(b, s)$ of nucleus A in a AA interaction. If $n_A(b, s) < n_{crit}$ the J/ψ is suppressed only due to ordinary nuclear absorption with cross-section σ_{abs} . On the contrary, if $n_A(b, s) \gtrsim n_{crit}$, the nuclear absorption formula is used with σ_{abs} infinity. In this way, no J/ψ can survive above the critical density. The deconfining approach leads to a satisfactory description of J/ψ suppression, with n_{crit} treated as a free parameter¹⁰. However, a quantitative analysis of the most recent NA50 data [37] is still missing. On the other hand, the centrality dependence of the average p_T of J/ψ is better described in the comovers approach than in a deconfining scenario [40].

7 Conclusions

In these lectures a description of microscopic string models of hadronic and nucleus interactions has been presented. Consequences of the model for charged particles multiplicities, net baryon production (stopping), hyperon and antihyperon production (strangeness enhancement) and J/ψ suppression have been examined.

As a starting point we have assumed that particles produced in different strings are independent, i.e. there is no ‘‘cross-talk’’ between strings. While this assumption works quite well in pp and pA interactions, the AA data can only be described if final state interaction (comovers interaction) is introduced. However, the corresponding cross-section turns out to be rather small (a few tenths of a milibarn). Due to this smallness and to the short duration time of final state interaction ($5 \div 7 \text{ fm}$) it is unlikely that thermal equilibrium can be reached.

¹⁰Both in the comovers model and in the deconfining one, the description of the J/ψ suppression at very large transverse energy, E_T , requires the introduction of E_T -fluctuations [30] [39].

Of course it is not possible to reach a definite conclusion on this important point. However, particle abundances not only do not allow to conclude that equilibrium has been reached, but, on the contrary, their centrality dependence tends to indicate that this is not the case. Let us consider for instance p and \bar{p} production. In our model, their yields are practically not affected by final state interaction, i.e. they are practically the same assuming string independence. Yet, the model reproduces the data, from very peripheral to very central interaction. This success would be difficult to understand in a QGP scenario in which for peripheral collisions (below the critical density) there is strong, non-equilibrated, $p\bar{p}$ annihilation, which becomes equilibrated for central ones, above the critical density. More generally, the QGP scenario would be strongly supported if some kind of threshold would be found in the strange baryon yields around the critical energy density. At SPS energies, evidence for such a threshold in the $\bar{\Xi}$ yield was claimed by the NA57 collaboration based on preliminary data [41], but it is not seen in the more recent analysis [42]. Moreover, the saturation at large centralities of the B and \bar{B} yields per participants, shown by the WA97 data, has also disappeared from the new data [42], in agreement with the predictions of the comovers interaction model [38]. Unfortunately, these data only cover a limited range of centrality. In contrast to this situation, the RHIC data explore the whole centrality range from very peripheral to very central collisions and the centrality dependence of the yields of p , Λ , Ξ and their antiparticles shows no structure whatsoever. Moreover, the yields of Ξ and $\bar{\Xi}$ per participant (as well as the ratios Ξ/h^- and $\bar{\Xi}/h^-$) do not seem to saturate at large centralities. If the same happens for Ω and $\bar{\Omega}$ production (as predicted in our approach, Figs. 16) the case for QGP formation from strange baryon enhancement will be quite weak.

Finally, it should be stressed that the final state interaction of comovers in our approach is by no means a trivial hadronic effect. Indeed, the interaction of comovers starts at the early times when densities, as computed in DPM, are very large. In this situation the comovers are not hadrons (there are several of them in the volume normally occupied by one hadron, and, moreover, at these early times hadrons are not yet formed). This is probably the reason why in our approach the comover interaction cross-sections required to describe the data are smaller than in hadron gas models where the final state interaction starts only after hadron formation.

Table 1: Calculated values [25] of the rapidity distribution of $pp \rightarrow p - \bar{p} + X$ at $\sqrt{s} = 17.2$ GeV and 27.4 GeV ($k = 1.4$) and $\sqrt{s} = 130$ GeV ($k = 2$). (In order to convert $d\sigma/dy$ into dN/dy a value of $\sigma = 30$ mb has been used). For comparison with the nucleus-nucleus results, all values in this table have been scaled by $n_A = 175$.

y^*	$pp \rightarrow p - \bar{p}$ $\sqrt{s} = 17.2$ GeV	$pp \rightarrow p - \bar{p}$ $\sqrt{s} = 27.4$ GeV	$pp \rightarrow p - \bar{p}$ $\sqrt{s} = 130$ GeV
0	9.2	6.5 [6.3 ± 0.9]	3.6
1	15.0 [16.1 ± 1.8]	9.3 [9.6 ± 0.9]	4.2
1.5	25.8 [24.1 ± 1.4]	14.6 [15.4 ± 0.9]	5.1
2	47.1 [45.4 ± 1.4]	26.2 [27.7 ± 0.9]	6.8

Appendix A

In order to get the relative densities of each baryon and antibaryon species we use simple quark counting rules [28] [31]. Denoting the strangeness suppression factor by S/L (with $2L + S = 1$), baryons produced out of three sea quarks (which is the case for pair production) are given the relative weights

$$I_3 = 4L^3 : 4L^3 : 12L^2S : 3LS^2 : 3LS^2 : S^3 \quad (\text{A.1})$$

for $p, n, \Lambda + \Sigma, \Xi^0, \Xi^-$ and Ω , respectively. The various coefficients of I_3 are obtained from the power expansion of $(2L + S)^3$.

For net baryon production, we have seen in Section 4 that the baryon can contain either one or two sea quarks. The first case corresponds to direct diquark fragmentation described by the second term of Eq. (22). The second case corresponds to diquark splitting, described by the first term of (22). In these two cases, the relative densities of each baryon species are respectively given by

$$I_1 = L : L : S \quad (\text{A.2})$$

for p, n and $\Lambda + \Sigma$, and

$$I_2 = 2L^2 : 2L^2 : 4LS : \frac{1}{2}S^2 : \frac{1}{2}S^2 \quad (\text{A.3})$$

for $p, n, \Lambda + \Sigma, \Xi^0$ and Ξ^- . The various coefficients in (A.2) and (A.3) are obtained from the power expansion of $(2L + S)$ and $(2L + S)^2$, respectively.

In order to take into account the decay of $\Sigma^*(1385)$ into $\Lambda\pi$, we redefine the relative rate of Λ 's and Σ 's using the empirical rule $\Lambda = 0.6(\Sigma^+ + \Sigma^-)$ – keeping, of course, the total yield of Λ 's plus Σ 's unchanged. In this way the normalization constants of all baryon species are determined from one of them. This constant, together with the relative normalization of K and π , are determined from the data for very peripheral collisions. In the calculations we use $S = 0.1$ ($S/L = 0.22$).

References

- [1] For a review see F. Karsch: hep-lat/0106019 and references therein
- [2] For a review see K. Rajagopalan: Nucl. Phys. **A661**, 150 c (1999) and references therein
- [3] T. Matsui, H. Satz: Phys. Lett. **178B**, 416 (1986)
- [4] See P. Braun-Munzinger: these proceedings and references therein
P. Koch, B. Muller, J. Rafelski: Phys. Rep. **142**, 167 (1986)
- [5] J. S. Hamich, K. Redlich, A. Tousi: Phys. Lett. B **486**, 61 (2000) and J. Phys. G **27**, 413 (2001)
- [6] F. Becattini, Z. Phys. C **69**, 485 (1996)
- [7] A. Capella, U. Sukhatme, C-I Tan, J. Tran Thanh Van: Phys. Rep. **236**, 225 (1994)
- [8] P. Aurenche, F. W. Bopp, A. Capella, P. Maire, J. Kwiecinski, J. Ranft, J. Tran Thanh Van: Phys. Rev. D **45**, 92 (1992)
- [9] A. Kaidalov, in: *QCD at 200 TeV*, L. Ciafarelli, Yu Dokshitzer eds, (Plenum Press, New York, 1992), p. 1
- [10] N. S. Amelin et al.: Sov. Jour. Nucl. Phys. **51**, 133 and 535 (1990) ; ibid **52**, 362 (1990)
- [11] V. N. Gribov: ZhETF **57**, 654 (1967)
M. Baker, A. K. Ter-Martirosyan: Phys. Rep. Phys. Rep. **28**, 1 (1976)
- [12] M. Froissart: Phys. Rev. **123**, 1053 (1961)
- [13] V. Abramovski, V. N. Gribov, O. Kancheli: Sov. J. Nucl. Phys. **18**, 308 (1974)

- [14] A. Capella, A. Kaidalov, J. Tran Thanh Van: Heavy Ion Physics **9** (1999)
N. Armesto, A. Capella, A. B. Kaidalov, J. Lopez-Albacete, C.A. Salgado,
hep-ph/0304119
- [15] T. Regge: Nuovo Cimento **14**, 951 (1959)
- [16] V. N. Gribov: ZhETF **41**, 667 (1961)
G. F. Chew, S. C. Frautschi: Phys. Rev. Lett. **7**, 394 (1961)
R. Blankenbecler, M. Goldberger: Phys. Rev. **126**, 766 (1962)
For a review see P. D. B. Collins: Phys. Rep **1C**, 105 (1970)
- [17] G. t'Hooft: Nucl. Phys. B **72**, 461 (1974)
- [18] G. Veneziano: Nucl. Phys. B **74**, 365 (1974)
- [19] G. Veneziano: Nucl. Phys. B **117**, 519 (1976)
- [20] M. Ciafaloni, G. Marchesini, G. Veneziano: Nucl. Phys. B **98**, 472 (1975)
- [21] A. Capella, D. Sousa: Phys. Lett. B **511**, 185 (2001)
- [22] A. Kaidalov: Yad Fiz **45**, 1452 (1987)
- [23] A. Capella, J. Kwiecinski, J. Tran Thanh Van: Phys. Lett. **108B**, 347 (1982)
A. Capella, C. Pajares, A. Ramallo: Nucl. Phys. B **241**, 175 (1984)
- [24] NA 49 collaboration, H. Appelshäuser et al: Phys. Rev. Lett. **82**, 2471 (1999)
- [25] A. Capella: Phys. Lett. B **542**, 63 (2002)
- [26] G. C. Rossi, G. Veneziano: Nucl. Phys. **123**, 507 (1977)
- [27] B. Z. Kopeliovich, B. G. Zakharov: Sov. J. Nucl. Phys. **48**, 136 (1988) ; Z.
Phys. C **43**, 241 (1989)
- [28] A. Capella, C. A. Salgado: New Journal of Phys. **2**, 30.1 (2000) ; Phys. Rev.
C **60**, 054906 (1999)
A. Capella, E. G. Ferreira, C. A. Salgado: Phys. Lett. **81B**, 68 (1979)
- [29] B. Koch, U. Heinz, J. Pitsut: Phys. Lett. **B243**, 149 (1990)
- [30] A. Capella, A. Kaidalov, D. Sousa: Phys. Rev. C **65**, 054908 (2002)
A. Capella, A. Kaidalov, E. G. Ferreira: Phys. Rev. Lett. **85**, 2080 (2000)
- [31] A. Capella, C. A. Salgado, D. Sousa: nucl-th/0205014
- [32] PHENIX collaboration, K. Adcox et al.: nucl-ex/0112006

- [33] STAR collaboration, C. Adler et al.: Phys. Rev. Lett. **87**, 262302 (2001)
- [34] STAR collaboration, J. Castillo: Proceedings Quark Matter 2002, Nantes, France
- [35] STAR collaboration, C. Adler et al.: Phys. Rev. Lett. **86**, 4778 (2001)
- [36] J. Ranft, A. Capella, J. Tran Thanh Van: Phys. Lett. B **320**, 346 (1999)
N. S. Amelin, N. Armesto, C. Pajares, D. Sousa: Eur. Phys. J. **C222**, 149 (2001)
- [37] NA50 collaboration, J. L. Ramello: Proceedings Quark Matter 2002, Nantes, France
NA50 collaboration, H. Santos: Proceedings XXXVIII Rencontres de Moriond, Les Arcs (France) 2003
- [38] A. Capella, D. Sousa: nucl-th/0303055
- [39] J. P. Blaizot, P. M. Dinh, J. Y. Ollitrault: Phys. Rev. Lett. **85**, 4012 (2000)
- [40] N. Armesto, A. Capella, E. G. Ferreira: Phys. Rev. **C59**, 345 (1999)
A. K. Chaudhuri, nucl-th/0212046
D. Kharzeev, M. Nardi, H. Satz: Phys. Lett. B **404**, 14 (1997)
- [41] NA57 collaboration, N. Carrer: Nucl. Phys. **A698**, 118c (2002)
- [42] NA57 collaboration, G. Bruno: Proceedings XXXVIII Rencontres de Moriond, Les Arcs (France) 2003
- [43] BRAHMS collaboration, P. Christiansen: nucl-ex/0212002

Figure captions

Figure 1 : Phase diagram in statistical QCD [1] [2].

Figure 2 : Energy density versus temperature in lattice QCD [1] at $\mu = 0$, for three light flavors (upper), two light and one heavier (middle) and two light flavors (lower).

Figure 3 : Single (a), double (b), and multiple (c) scattering diagrams in the eikonal model.

Figure 4 : The secondary Regge trajectories with highest intercept.

Figure 5 : The mechanism of particle production in e^+e^- annihilation. The net of soft gluons and quark loops is only shown here and in Fig. 10.

Figure 6 : One string diagram in $\bar{p}p$.

Figure 7 : Dominant two-chain (single cut Pomeron) contributions to high energy π^+ -proton collisions.

Figure 8 : Dominant two-chain contribution to proton-antiproton collisions at high energies (single cut Pomeron).

Figure 9 : Dominant two-chain diagram describing multiparticle production in high energy proton-proton collisions (single cut Pomeron).

Figure 10 : Single Pomeron exchange and its underlying cylindrical topology. This is the dominant contribution to proton-proton elastic scattering at high energies.

Figure 11 : Two cut Pomeron (four-chain) diagram for proton-proton collisions.

Figure 12 : The values of dN^{ch}/dy per participant for $Pb Pb$ collisions at $\sqrt{s} = 17.3$ GeV computed [21] from Eq. (19), compared with WA98 data.

Figure 13 : The values of $dN^{ch}/d\eta_{c.m.}/(0.5 n_{part})$ for $Au Au$ collisions at $\sqrt{s} = 130$ GeV computed [21] from Eq. (19) including shadowing corrections are given by the dark band in between solid lines. The PHENIX data are also shown (black circles and shaded area).

Figure 14 : Rapidity distribution of net protons ($p-\bar{p}$) for the 5 % most central $Pb Pb$ collisions at SPS ($\sqrt{s} = 17.2$ GeV) and for the 10 % most central $Au Au$ ones at $\sqrt{s} = 200$ GeV, compared to data [24] [43].

Figure 15 : (a) Calculated values [31] of dN/dy of p (solid line) \bar{p} (dashed line), and $p - \bar{p}$ (dotted line) at mid rapidities, $|y^*| < 0.35$, are plotted as a function of $dN_{h-}/d\eta$, and compared with PHENIX data [32] ; (b) same for Λ and $\bar{\Lambda}$ compared

with preliminary STAR data [33] ; (c) same for Ξ^- and Ξ^+ compared to preliminary STAR data [34] ; (d) same for Ω and $\bar{\Omega}$.

Figure 16 : Calculated values [31] of the ratios B/n_{part} (a) and \bar{B}/n_{part} (b), normalized to the same ratio for peripheral collisions ($n_{part} = 18$), plotted as a function of n_{part} .

Figure 17 : The ratio of J/ψ over DY cross-sections in $Pb Pb$ collisions a 158 GeV/c versus E_T obtained [38] in the comovers interaction model with $\sigma_{abs} = 4.5$ mb and $\sigma_{co} = 0.65$ mb. The absolute normalization is 47. The preliminary data are from [37].

Figure 18 : dN/dy of J/ψ (times branching ratio) in $Au Au$ collisions at $\sqrt{s} = 200$ GeV per nucleon and $y^* \sim 0$, scaled by the number of binary collisions $\langle nb \rangle$, versus the number of participants. The curves are obtained in the comovers model [38] with $\sigma_{abs} = 0$, $\sigma_{co} = 0.65$ mb (upper) and $\sigma_{abs} = 4.5$ mb, $\sigma_{co} = 0.65$ mb (lower). The absolute normalization is arbitrary. An extra 20 % suppression between pp and central $Au Au$ is expected due to shadowing.

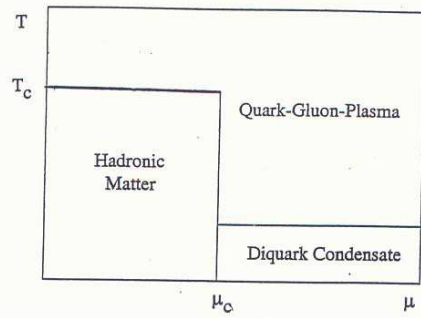


Fig. 1

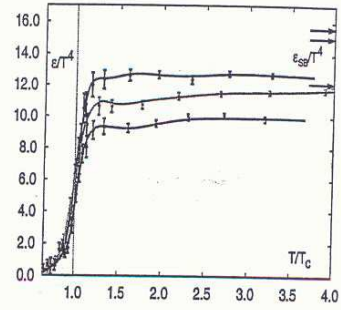


Fig. 2

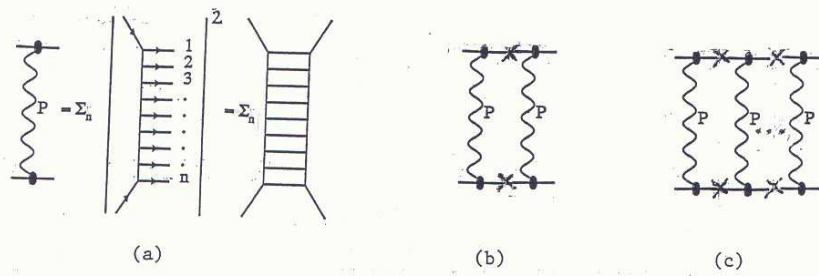


Fig. 3

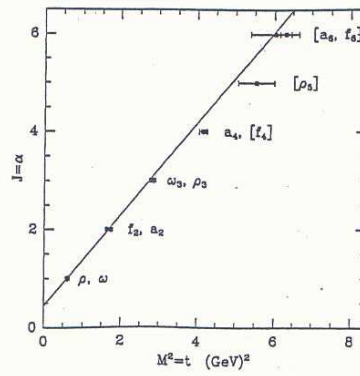


Fig. 4

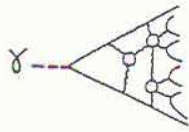


Figure 5

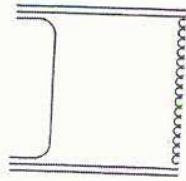


Figure 6

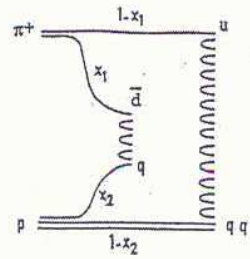


Figure 7

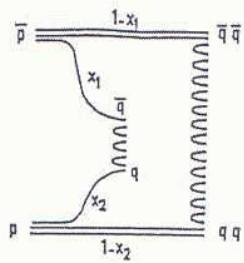


Figure 8

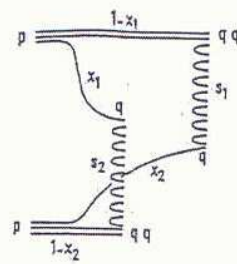


Figure 9

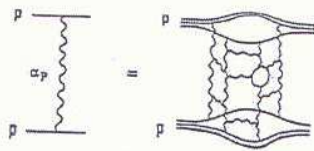


Figure 10

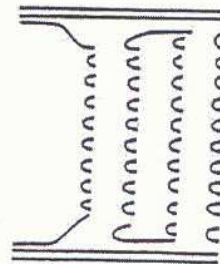


Figure 11

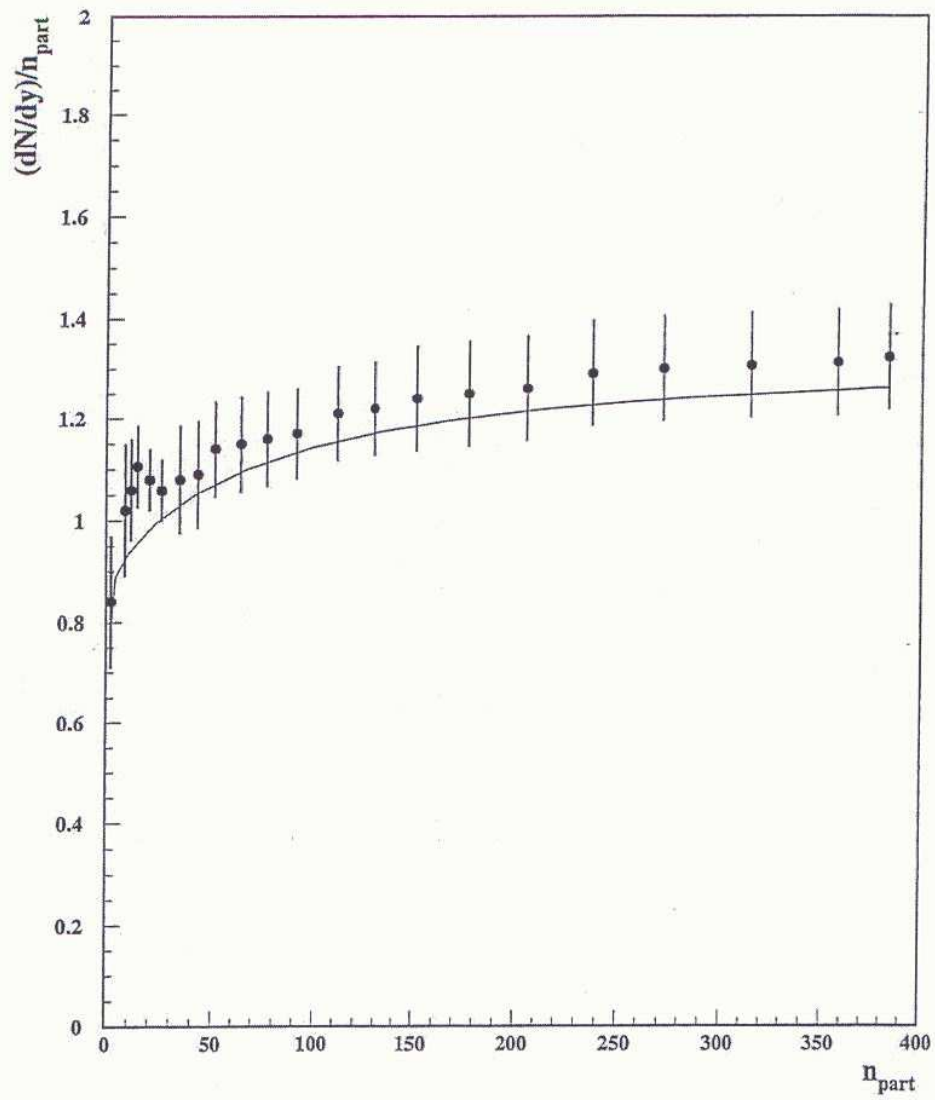


Figure 12

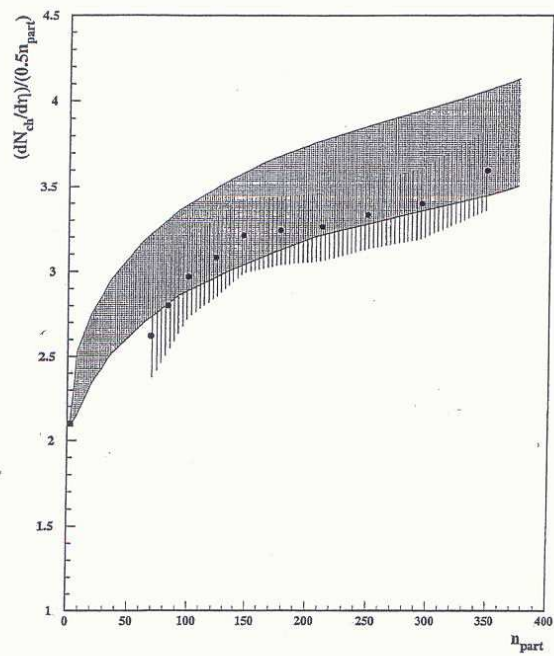


Fig. 13

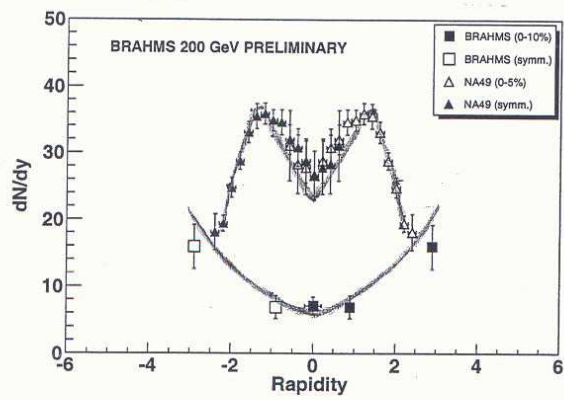


Fig. 14

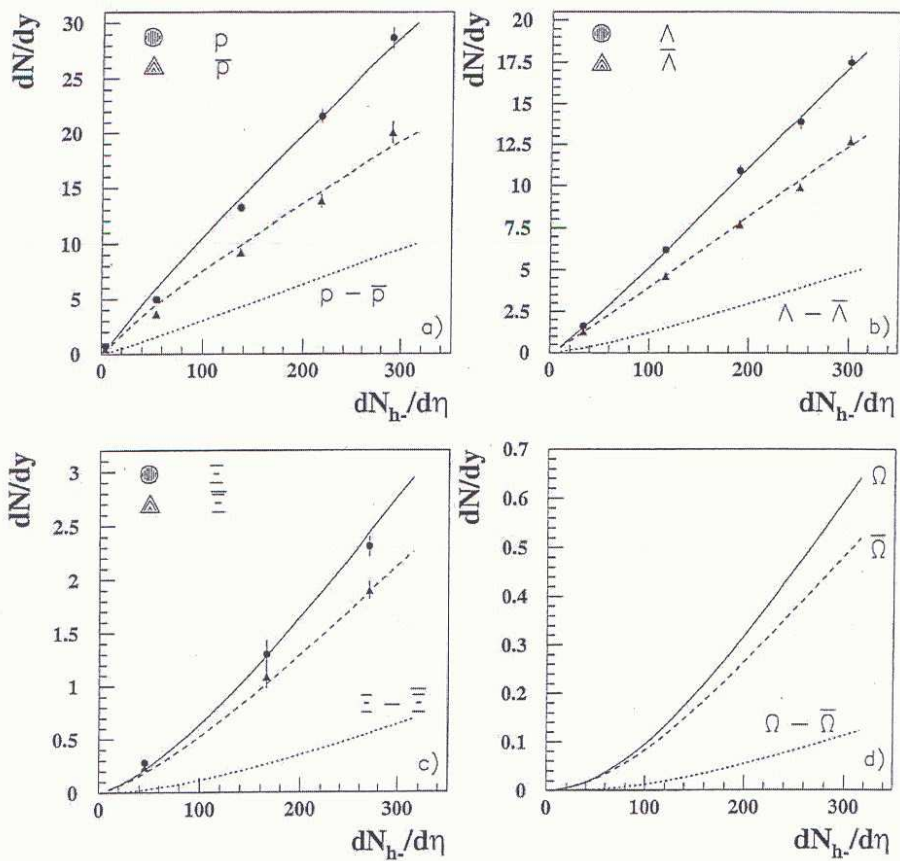


Figure 15

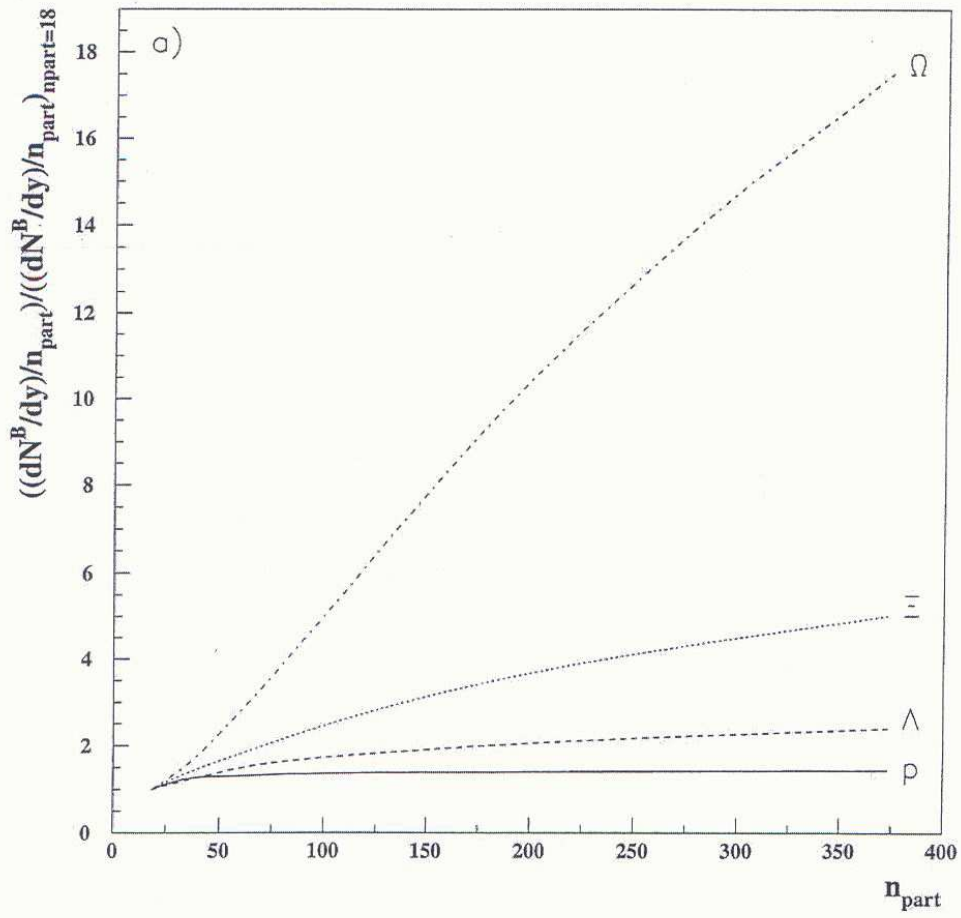


Figure 16a

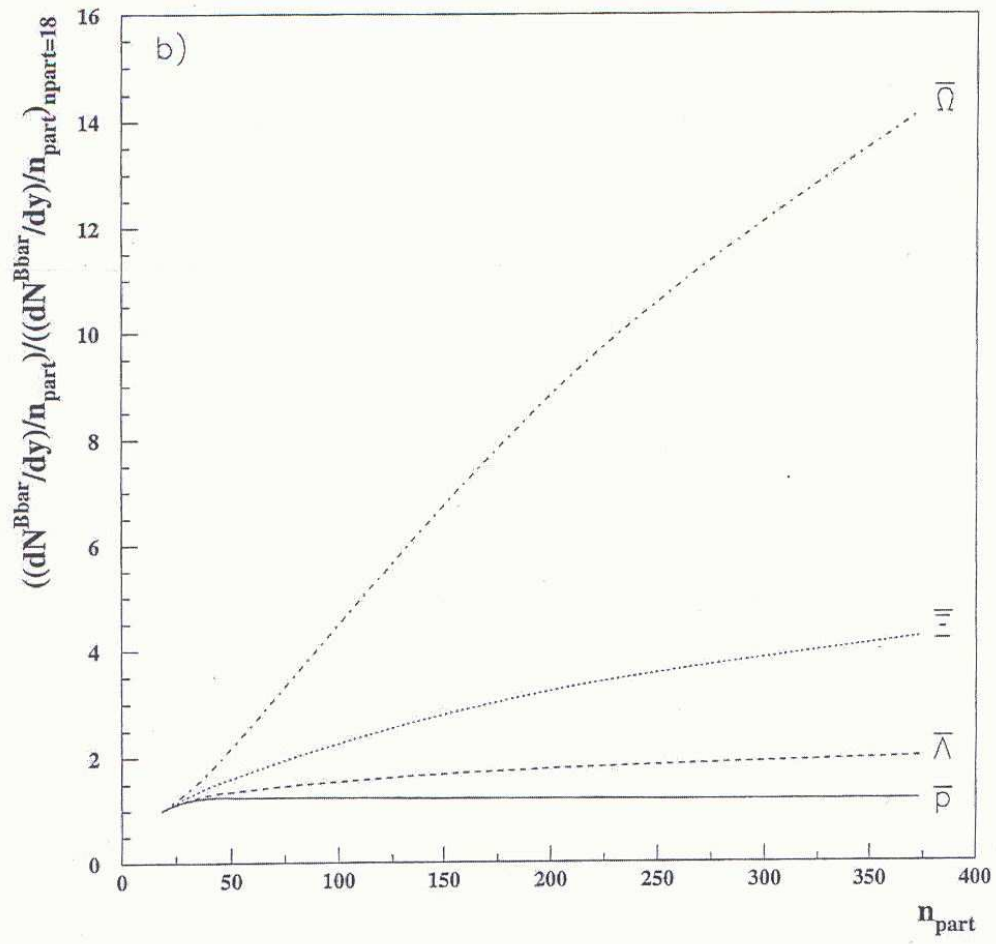


Figure 16b

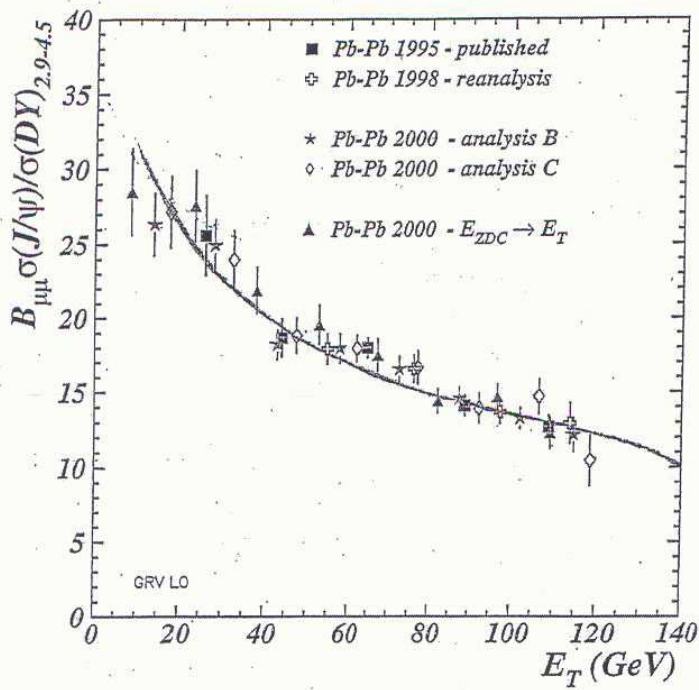


Figure 17

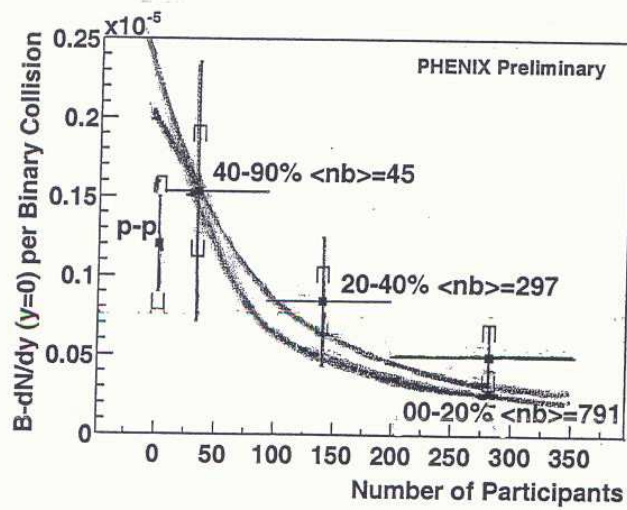


Fig. 18